nature materials

SUPPLEMENTARY INFORMATION

DOI: 10.1038/NMAT3409

Spin excitations in a single La_2CuO_4 layer

Here we describe how the films were synthesized using molecular beam epitaxy and their characterization using reflection high-energy-electron diffraction, atomic force microscopy, x-ray reflectivity, x-ray absorption and muon spin rotation.

I. SAMPLE PREPARATION METHODS

The films were synthesized using a unique atomic layer-by-layer molecular-beam epitaxy (ALL-MBE) system at Brookhaven National Laboratory (BNL) [1]. The system features sixteen elemental metal sources (thermal effusion Knudsen cells). The source rates were calibrated using a quartz crystal oscillator and measured in real-time using a custom-built 16-channel atomic absorption spectroscopy system [2]. Each source is provided with a computer-controlled pneumatic shutter; the updated rates are used to calculate the shuttering times that correspond to the desired sequence of atomic monolayers. To double-check the absolute deposition rates the film thickness was measured after growth using x-ray reflectivity.

The seventeenth source is a custom-built ozone distiller system which supplies pure ozone gas. Since its oxidation power is much higher than that of O_2, ozone can fully oxidize copper even at very low partial pressure ($p = 10^{-6}$ to 10^{-5} Torr, depending on the temperature). This allows synthesis of high-quality cuprate films under high vacuum conditions, which in turn enables one to use surface-science tools such as reflection high-energy-electron diffraction (RHEED) and time-of-flight ion-scattering and recoil spectroscopy, both of which are implemented in the BNL MBE system. These tools provide information about the surface crystalline structure and chemical composition, *in-situ* and during the film growth, which facilitates further fine-tuning of the film stoichiometry and morphology [1].

Using the ALL-MBE technique and the above suite of analytical tools, we reproducibly fabricate single-crystal films of cuprate superconductors and other complex oxides, with atomically smooth surfaces and interfaces. We have also synthesized a large variety of precise heterostructures, multilayers and superlattices. Many of these contain layers that are just one unit cell (1 UC) thick; indeed, we have demonstrated the capability to fabricate

DOI: 10.1038/NMAT3409

1 UC thick insulating barrier layers without pinholes over macroscopic areas[1] as well as 1 UC thick superconducting films with T_c as high as in the best bulk samples [3–5].

For the present study, the films were grown on $10 \times 10 \times 1$ mm^3 single-crystal $LaSrAlO_4$ substrates with the large surfaces polished perpendicular to the [001] direction. During growth, the chamber pressure was kept fixed at $p = 9 \times 10^{-6}$ Torr of ozone and the substrate temperature $T_s \approx 700$°C. After the growth was completed, the sources were closed, the substrate temperature and the ozone pressure, p, were raised to $T_s \approx 760$°C and $p = 2.5 \times 10^{-5}$ Torr and the sample given a short anneal in situ; this we have found to improve the crystalline coherence as inferred from x-ray diffraction measurements, although at the expense of somewhat increased surface roughness. Subsequently, the films were cooled at the same ozone pressure down to a lower temperature ∼300°C, and then in high vacuum $p < 1 \times 10^{-7}$ Torr down to room temperature. Every film was subsequently annealed under high vacuum to drive out all the interstitial oxygen and avoid inadvertent oxygen doping. Details including the source temperatures and rates, the layering sequence, the substrate temperature, etc., are given in Table 1 for each of the three films reported here.

The quality of the film growth was checked in real time by monitoring RHEED pattern dynamics as well as intensity oscillations, which provide digital information on the film thickness. In Figs. 1-3, we show representative RHEED diffractograms. There are apparent differences between the diffractograms recorded after the deposition of an AlO_2, CuO_2, or LaO layer. For the AlO_2 layer, a RHEED pattern is observed (Fig. 1), showing streaks that originate from Bragg diffraction peaks with large Scherrer broadening along the z-axis due to the grazing angle incidence of the electron beam and steps on the surface. The distance between the streaks corresponds to the in-plane lattice constant of about 3.8 Å. During deposition of each CuO_2 layer, four additional weaker side-bands appear (Fig. 2) in-between each pair of main Bragg reflections. This indicates a fivefold increase of the in-plane lattice constant, i.e. a 5×5 surface reconstruction (verified by rotating the sample by 90°). After depositing an LaO layer, the side-bands disappear (Fig. 3) but one can observe a strong modulation of the intensity along the main streaks; evidence of transmission originating from some three-dimensional asperities on the surface. Apparently, the surface gets rougher after each LaO layer due to some tendency for 3D growth and island formation; however, these (very small) islands are covered or dissolved by subsequent AlO_2 or CuO_2 layers, which restore an atomically smooth surface.

Table 1.

25 x [1UC $LaAlO_3$ + 1 UC La_2CuO_4]

Source	temperature [^{0}C]	rate [ML/s][a]
La-1	1574	0.0098
La-2	1563	0.0101
Cu-1	1208/1138	0.0095
Cu-2	1210/1140	0.0104
Al-1	1170	0.0166

Substrate temperature[b]	674^{0}C
Chamber pressure	9x10^{-6} Torr
Growth sequence:	{ 1ML of La / 1ML of Al / pause 20 sec. / (2ML of La / 1ML of Cu / pause 20 sec.) repeated twice }, repeated 25 times.
In-situ ozone annealing	
time	20 min.
temperature	735^{0}C
ozone pressure	2.5x10^{-5} Torr
ozone shut-off temperature	330^{0}C
Ex-situ vacuum annealing	
time	300 min.
temperature	250^{0}C
pressure	1.6x10^{-6} Torr
cool down	overnight
AFM surface roughness[c]	< 0.3 nm

15 x [2UC $LaAlO_3$ + 2 UC La_2CuO_4]

Source	temperature [^{0}C]	rate [ML/s]
La-1	1574	0.0098
La-2	1563	0.0102
Cu-1	1209/1139	0.0102
Cu-2	1211/1141	0.0102
Al-1	1150	0.0156

Substrate temperature[b]	670^{0}C
Chamber pressure	9x10^{-6} Torr
Growth sequence:	{ (1ML of La / 1ML of Al / pause 20 sec.) repeated twice; (2ML of La / 1ML of Cu / pause 20 sec.) repeated four times}, the above recipe repeated 15 times.
In-situ ozone annealing	
time	26 min.
temperature	729^{0}C
ozone pressure	2.5x10^{-5} Torr
ozone shut-off temperature	315^{0}C

DOI: 10.1038/NMAT3409

Ex-situ vacuum annealing	
time	300 min
temperature	250^0C
pressure	$1.6\text{x}10^{-6}$ Torr
cool down	overnight
AFM surface roughness[c]	< 0.3 nm

40 UC La_2CuO_4

Source	temperature [^{0}C]	rate [ML/s]
La-1	1600	0.0287
La-2	1600	0.0235
Cu-1	1220/1150	0.0173
Cu-2	1260/1190	0.0186

Substrate temperature[b]	656^0C
Chamber pressure	$7\text{x}10^{-6}$ Torr
Growth sequence:	[2ML of La / 1ML of Cu / pause 20 sec.] repeated 40 times.
Cool down procedure:	
ozone pressure	$2.0\text{x}10^{-5}$ Torr
ozone shut-off temperature[d]	500^0C
AFM surface roughness[c]	< 0.6 nm

Notes.

[a] *ML = atomic monolayer.*
[b] *All quoted substrate temperatures are nominal pyrometer readings (not corrected for emissivity).*
[c] *Rms surface roughness was measured over 10x10 μm^2 area and is inclusive of substrate steps, occasional dust particles, etc.*
[d] *The sample was slowly cooled down in high vacuum ($p < 10^{-7}$ Torr) from 500^0C to room temperature.*

Another way to observe the dynamics of surface roughening and smoothing is by measuring the brightness of the specular reflection spot as a function of time. As seen in Fig.4, it exhibits pronounced oscillations, in agreement with the pattern-changing dynamics discussed above. Note that RHEED oscillations allow for digital control of the number of monolayers in films, hetero-structures and superlattices.

After the growth, every film was characterized ex situ by atomic force microscopy (AFM), high-resolution x-ray diffraction (XRD), resistivity, x-ray absorption spectroscopy and muon spin rotation.

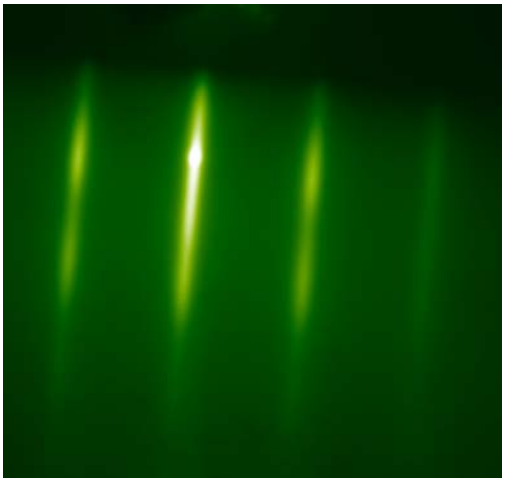

FIG. 1. RHEED pattern recorded during growth of 25×[$LaAlO_3$ + La_2CuO_4], immediately after an AlO_2 layer has been deposited.

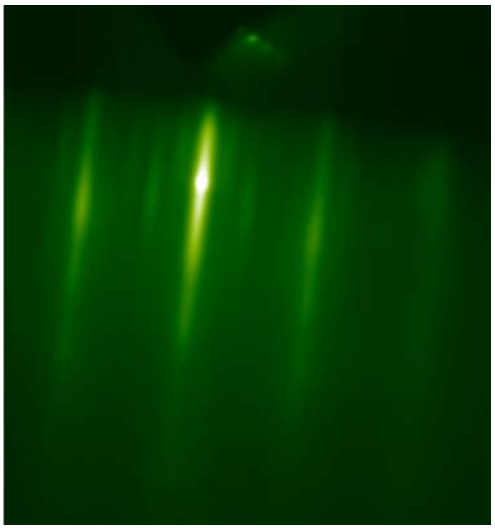

FIG. 2. RHEED pattern recorded during growth of 25×[$LaAlO_3$ + La_2CuO_4], immediately after an CuO_2 layer has been deposited.

DOI: 10.1038/NMAT3409

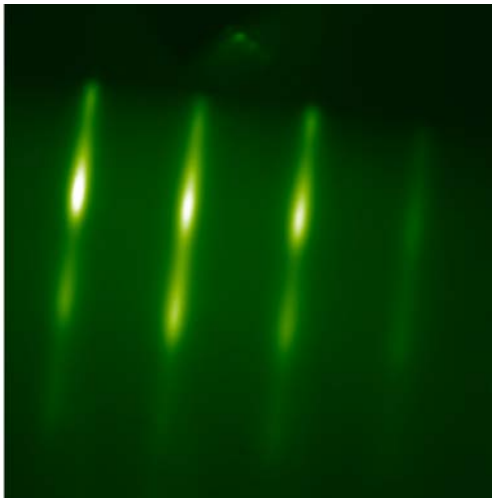

FIG. 3. RHEED pattern recorded during growth of 25×[$LaAlO_3$ + La_2CuO_4], immediately after an CuO_2 layer has been deposited.

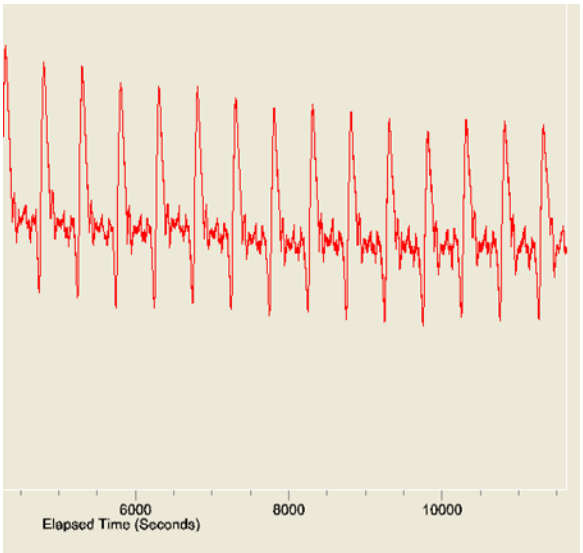

FIG. 4. RHEED oscillations (intensity of the specular reflection measured as a function time) recorded during growth of 25×[$LaAlO_3$ + La_2CuO_4].

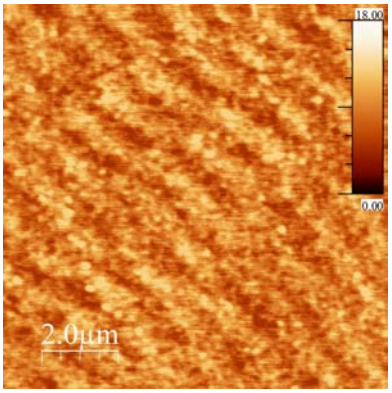

FIG. 5. AFM image of 25×[$LaAlO_3$ + La_2CuO_4]. The rms surface roughness is 0.3 nm.

II. ATOMIC FORCE MICROSCOPY

Fig. 5 shows a typical AFM image of 25×[$LaAlO_3$ + La_2CuO_4], similar also to those of Samples B and C. The surface is smooth, without any secondary-phase precipitates. The measured root-mean-square (rms) roughness of the surface, over a large (100 μm^2) area, is 0.3 nm. This is inclusive of occasional steps, half-a-unit cell (0.6 nm) tall, that originate from the slight miscut ($\sim 0.1^\circ$) of the substrate away from the targeted surface perpendicular to the crystallographic (001) direction. On the terrace, between two steps, the rms roughness is smaller than 0.1 nm i.e., the surface is atomically smooth. This is very similar to what we see in bare $LaSrAlO_4$ substrates.

III. X-RAY REFLECTIVITY AND X-RAY ABSORPTION

The results of x-ray reflectivity measurements, plotted in Fig. 6, show oscillations over 8 orders of magnitude in intensity. Fitting the data using the GenX software [6] reveals sharp interfaces with an estimated rms roughness of 0.6 nm. Due to the similar densities of La_2CuO_4 and $LaAlO_3$, the statistical uncertainty of the thickness of individual La_2CuO_4 and $LaAlO_3$ layers is $\sim$0.1 nm, and within this error the thicknesses of 1.32 nm and 0.38 nm are consistent with the bulk data. X-ray diffraction data showed that the films are pseudomorphic with the $LaSrAlO_4$ substrate, i.e., the in-plane lattice constants in the film are equal to those of the substrate (a_0= 3.755 Å). Hence, the films are under compressive strain, about -1.2% for La_2CuO_4 (pseudo-cubic a_0 3.803 Å) and -1.0% for $LaAlO_3$ (a_0= 3.793 Å).

Given that atomic diffusion or electronic reconstructions sometimes cause doping effects

DOI: 10.1038/NMAT3409

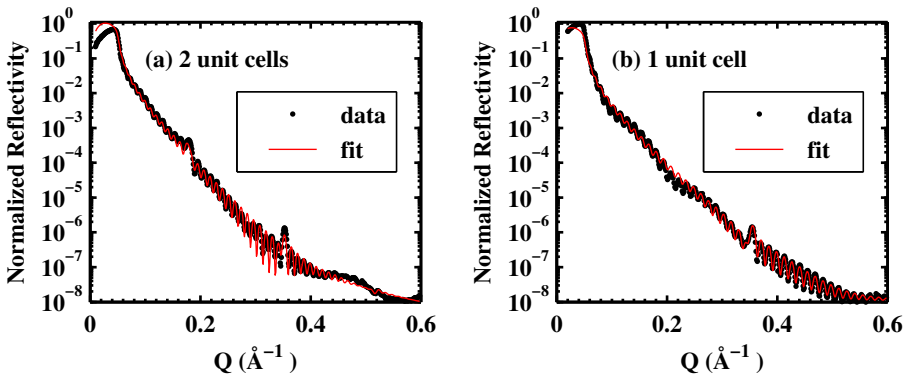

FIG. 6. The normalized x-ray reflectivity profiles for (a) the two unit cell film (15×[2 $LaAlO_3$ + 2La_2CuO_4]) and (b) the 1 unit cell film (25×[$LaAlO_3$ +La_2CuO_4]).

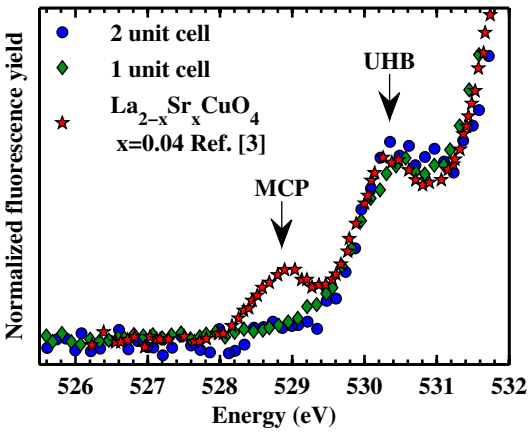

FIG. 7. The x-ray absorption of the 2 unit cell film (15×[2 $LaAlO_3$ + 2La_2CuO_4]) (blue ○) and 1 unit cell film (25×[$LaAlO_3$ + La_2CuO_4]) (green◇) films contrasted with data for $La_{2-x}Sr_xCuO_4$ $x = 0.04$ from Ref. [8] (red ⋆). Arrows mark the mobile carrier peak (MCP) and the upper Hubbard band (UHB).

at oxide interfaces [7], it is important to confirm that these effects are not present in our films. To do this, we measured the O K-edge x-ray absorption fluorescence yield as shown in Fig. 7, which compares our films to a Sr doped sample from Ref. [8]. Doping holes into La_2CuO_4 is known to give rise to an additional prepeak in the spectrum, known as the mobile carrier peak[8]. The absence of this peak demonstrates negligible doping in the present case. Transport measurements also verified that the films were insulating as intended.

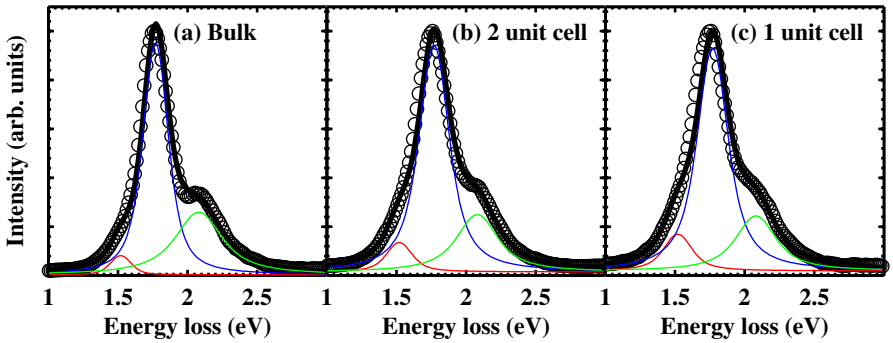

FIG. 8. A comparison of the dd-excitation in the (a) bulk, (b) 2 unit cell ((15×[2 $LaAlO_3$ + 2 La_2CuO_4])) and (c) 1 unit cell ((25×[$LaAlO_3$ +La_2CuO_4])) films measured at $\boldsymbol{Q} = (0, 0)$ (black ○). The black line is the fit composed of contributions from the $3z^2 - r^2$ (red), xy (blue), and xz/yz(green) orbitals.

IV. ELECTRONIC *DD*-EXCITATIONS

During the RIXS measurements, we have an additional check of the sample integrity, because in addition to the magnetic excitations, local electronic excitations termed*dd*-excitations are present in every RIXS spectrum we collected. These excitations are visible in the 1-3 eV energy loss window of the RIXS spectra [9] and correspond to excitations for which the $x^2 - y^2$ hole on the Cu atoms is excited into another orbital. Figure 8 provides a representative example, comparing the dd-excitations in the bulk, 2uc, and 1uc films measured at $\boldsymbol{Q} = (0, 0)$[10]. We fit all measured spectra with a sum of 3 Lorentzian lineshapes corresponding to the $3z^2 - r^2$, xy, and xz/yz orbitals convolved with the experimental resolution. We find no measurable dispersion and obtain energies of 1.52(2), 1.77(2), and 2.08(2) eV for the $3z^2 - r^2$, xy, and xz/yz orbitals respectively. There is a slight broadening in the 1uc and 2uc films with respect to the bulk, which likely reflects a small strain variation. However, the overall spectral profiles are very similar in the three films and all the orbital energies are the same within the fitting accuracy of 0.02 eV. Given that the *dd*-excitations are highly sensitive to the Cu atoms' local atomic configuration [9], these results show that 1uc and 2uc films are a good realization of single and bilayer La_2CuO_4.

DOI: 10.1038/NMAT3409

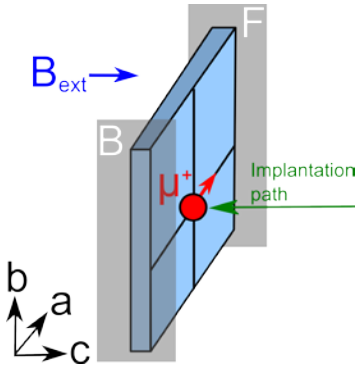

FIG. 9. The geometry for the muon spin rotation experiments at the LEM instrument, showing the directions of the muon spin and the applied external field. a, b and c refer to the crystalline axes of the sample and F and B are the detectors, which measure the positron emission from the muon decay.

V. MUON SPIN ROTATION

Muon spin rotation spectroscopy was performed at the LEM instrument at the Swiss Muon Source, Paul Scherrer Institut, Switzerland [11] in order to probe the magnetic properties of the films and to check that the different La_2CuO_4 units in the film are sufficiently isolated by the $LaAlO_3$ layers. The experimental geometry is shown in Fig. 9. Low energy ∼5-6 keV muons were implanted into the samples, such that the muon stopping profile roughly matched the film thickness. An external field of $\mathbf{B}_{\rm ext} = 3$ mT was applied along the c-axis of the film, perpendicular to the muon spin. The resulting time-dependent muon polarization distribution $A_0P(t)$ was measured as a function of temperature. For the case of a weak applied field, $A_0P(t)$ can be decomposed in transverse and longitudinal components with amplitudes A_T and A_L which are the amplitude of the precessing and of the non-precessing part of the polarization, respectively. Their temperature dependence reflects the build-up of local fields suppressing the precession around $\mathbf{B}_{\rm ext} = 3$ mT [12]. A_L and A_T provide information about the "static" (on microsecond scale) local field muons see at their implantation site on a length scale of ∼50 Å.

The renormalized classical model for the behavior of a 2D Heisenberg antiferromagnet predicts that the in-plane magnetic correlation length, $\xi_{\|}(T)$, and the magnetic correlation time will get exponentially larger as the temperature, T, is reduced. If successive 2D layers of a Heisenberg magnet are coupled by a small exchange constant $J_{\perp}$, the system will order

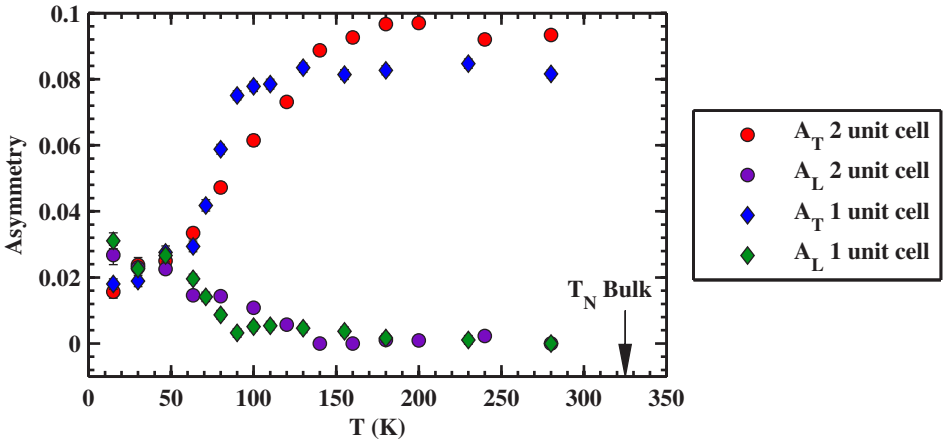

FIG. 10. The muon spin rotation the asymmetries A_T and A_L of the 2 unit cell (15×[2 $LaAlO_3$ + 2 La_2CuO_4]) and 1 unit cell films (25×[$LaAlO_3$ +La_2CuO_4]). Arrows denote the bulk La_2CuO_4 order temperature $T_N = 325$ K[14].

magnetically with a Néel transition temperature of [13]

$$k_B T_N \approx J_\perp \left(\frac{\xi_\parallel(T)}{a} \right)^2 . \quad (1)$$

At this phase transition A_T and A_L would show a pronounced increase and decrease, respectively [12]. As the layers are decoupled, T_N is suppressed and the renormalized classical model predicts that the correlation length and time will diverge at $T = 0$ K. La_2CuO_4 is widely belived to be a good realization of a Heisenberg antiferromagnet, but there may be subtle deparatures from this idealized model in real cuprates [14].

Figure 10 plots the evolution of the muon fit parameters for the 1 and 2 unit cell films. We see A_L and A_T begin to change around 100 K, well below the bulk ordering temperature of 325 K. They continue to evolve smoothly as the temperature is reduced, and at 15 K they are reduced by 80% . These results show that these films contain magnetically ordered patches with length scales $\xi_\parallel \gtrsim 50$ Å which persist on time scales of μs or longer. As muons are not sensitive to longer length scales or time scales than this, one cannot use these data to comment on the presence of long-range order, but these results are consistent with our expectations for isolated La_2CuO_4 layers and substantially different to bulk La_2CuO_4.

To investigate whether the $LaAlO_3$ buffer layer properly decouples the active La_2CuO_4layers we compare the 1 unit cell film (25×[$LaAlO_3$ + La_2CuO_4]) to the 2 unit cell film (15×[2 $LaAlO_3$ + 2 La_2CuO_4]). To do this, we define a characteristic temperature scale, $T_{\rm mag}$, as

DOI: 10.1038/NMAT3409

the point where A_T drops by 50% of its high temperature value. If magnetic superexchange were to give rise to significant coupling through the $LaAlO_3$ layers, $J_\perp$ and T_{mag} should decrease exponentially with the thickness of the $LaAlO_3$ layer. This is because the strength of superexchange scales as t^n where t is the hopping parameter and n is the number of bonds (other coupling mechanisms such as direct dipole coupling are also strong functions of $LaAlO_3$ thickness). So if interlayer coupling was significant, T_{mag} would be higher in the 1 unit cell film ($25\times$[$LaAlO_3$ +La_2CuO_4]) because this has a $LaAlO_3$ layer half as thick as the 2 unit cell film ($15\times$[2 $LaAlO_3$ + 2 La_2CuO_4]). Instead T_{mag} is higher in the two unit cell film than the 1 unit cell film (90 K compared to 76 K), implying that T_{mag} depends on the number of neighboring La_2CuO_4 unit cells in each layer more strongly than the thickness of the spacer layer, consistent with decoupled La_2CuO_4planes.

[1] I. Božović, G. Logvenov, M. A. J. Verhoeven, P. Caputo, E. Goldobin, and T. H. Geballe, Nature **422**, 873 (2003).

[2] M. E. Klausmeier-Brown, J. N. Eckstein, I. Bozovic, and G. F. Virshup, Applied Physics Letters **60**, 657 (1992).

[3] A. Gozar, G. Logvenov, L. F. Kourkoutis, A. T. Bollinger, L. a. Giannuzzi, D. A. Muller, and I. Božović, Nature **455**, 782 (2008).

[4] G. Logvenov, A. Gozar, and I. Božović, Science **326**, 699 (2009).

[5] A. T. Bollinger, G. Dubuis, J. Yoon, D. Pavuna, J. Misewich, and I. Bozovic, Nature **472**, 458 (2011).

[6] M. Björck and G. Andersson, J Appl. Cryst. **40**, 1174 (2007).

[7] J. Mannhart and D. G. Schlom, Science **327**, 1607 (2010).

[8] C. Chen, F. Sette, Y. Ma, M. Hybertsen, E. Stechel, W. Foulkes, M. Schulter, S.-W. Cheong, A. Cooper, L. Rupp, B. Batlogg, Y. Soo, Z. Ming, A. Krol, and Y. Kao, Phys. Rev. Lett. **66**, 104 (1991).

[9] M. M. Sala, V. Bisogni, C. Aruta, G. Balestrino, H. Berger, N. B. Brookes, G. M. de Luca, D. D. Castro, M. Grioni, M. Guarise, P. G. Medaglia, F. M. Granozio, M. Minola, P. Perna, M. Radovic, M. Salluzzo, T. Schmitt, K. J. Zhou, L. Braicovich, and G. Ghiringhelli, New J. Phys. **13**, 043026 (2011).

[10] We plan to report a complete, detailed analysis of the dd-excitations in a separate publication.

[11] E. Morenzoni, T. Prokscha, A. Suter, H. Luetkens, and R. Khasanov, Journal of Physics: Condensed Matter **16**, S4583 (2004).

[12] F. L. Pratt, Journal of Physics: Condensed Matter **19**, 456207 (2007).

[13] S. Chakravarty, B. Halperin, and D. Nelson, Phys. Rev. B **39**, 2344 (1989).

[14] M. A. Kastner, R. J. Birgeneau, G. Shirane, and Y. Endoh, Rev. Mod. Phys. **70**, 897 (1998).